Quantifying the impact of aerosol scattering on the retrieval of methane from airborne remote sensing measurements

Yunxia Huang[1,2], Vijay Natraj[3], Zhaocheng Zeng[2,4], Pushkar Kopparla[5], and Yuk L. Yung[2,3]

[1]School of Science, Nantong University, Nantong, 226007, China

[2]Division of Geological and Planetary Sciences, California Institute of Technology, Pasadena, CA 91125, USA

[3]Jet Propulsion Laboratory, California Institute of Technology, Pasadena, CA 91109, USA

[4]Joint Institute for Regional Earth System Science and Engineering, University of California, Los Angeles, CA 90095, USA

[5]Graduate School of Frontier Sciences, The University of Tokyo, Kashiwa, Chiba 277-0882, Japan

Correspondence to: Vijay Natraj (vijay.natraj@jpl.nasa.gov)

Abstract. As a greenhouse gas with strong global warming potential, atmospheric methane (CH_4) emissions have attracted a great deal of attention. Although remote sensing measurements can provide information about CH_4 sources and emissions, accurate retrieval is challenging due to the influence of atmospheric aerosol scattering. In this study, imaging spectroscopic measurements from the Airborne Visible/Infrared Imaging Spectrometer–Next Generation (AVIRIS-NG) in the short-wave infrared are used to compare two retrieval techniques — the traditional Matched Filter (MF) method and the Optimal Estimation (OE) method, which is a popular approach for trace gas retrievals. Using a numerically efficient two-stream-exact-single-scattering radiative transfer model, we also simulate AVIRIS-NG measurements for different scenarios and quantify the impact of aerosol scattering in the two retrieval schemes by including aerosols in the simulations but not in the retrievals. The presence of aerosols causes an underestimation of CH_4 in both the MF and OE retrievals; the biases increase with increasing surface albedo and aerosol optical depth (AOD). Aerosol types with high single scattering albedo and low asymmetry parameter (such as water soluble aerosols) induce large biases in the retrieval. When scattering effects are neglected, the MF method exhibits lower fractional retrieval bias compared to the OE method at high CH_4 concentrations (2–5 times typical background values), and is suitable for detecting strong CH_4 emissions. For an AOD value of 0.3, the fractional biases of the MF retrievals are

34 between 1.3 and 4.5%, while the corresponding values for OE retrievals are in the 2.8–5.6% range. On

35 the other hand, the OE method is an optimal technique for diffuse sources (<1.5 times typical background

36 values), showing up to five times smaller fractional retrieval bias (8.6%) than the MF method (42.6%)

37 for the same AOD scenario. However, when aerosol scattering is significant, the OE method is superior

38 since it provides a means to reduce biases by simultaneously retrieving AOD, surface albedo and CH_4.

39 The results indicate that, while the MF method is good for plume detection, the OE method should be

40 employed to quantify CH_4 concentrations, especially in the presence of aerosol scattering.

1 Introduction

Atmospheric methane (CH_4) is about 85 times more potent per unit mass at warming the Earth than carbon dioxide (CO_2) on a 20-year timescale (IPCC, 2013), implying that reduction in CH_4 emissions could be very efficient to slow down global warming in the near term. Global mean CH_4 concentrations have increased from ~700 ppb in the preindustrial era to more than 1860 ppb as of 2019 (NOAA, 2019). The most effective sink of atmospheric CH_4 is the hydroxyl radical (OH) in the troposphere. CH_4 reacts with OH to reduce the oxidizing capacity of the atmosphere and generate tropospheric ozone. Increasing emissions of CH_4 reduce the concentration of OH in the atmosphere. With less OH to react with, the lifespan of CH_4 could also increase, resulting in greater CH_4 concentrations (Holmes et al., 2013). Soils also act as a major sink for atmospheric methane through the methanotrophic bacteria that reside within them.

Significant natural CH_4 sources include wetlands (Bubier et al., 1994, Macdonald et al., 1998; Gedney et al., 2004), geological seeps (Kvenvolden and Rogers, 2005; Etiope et al., 2009), ruminant animals, and termites. In addition, increased surface and ocean temperatures associated with global warming may increase CH_4 emissions from melting permafrost (Woodwell et al., 1998; Walter et al., 2006; Schaefer et al., 2014, Schuur et al., 2015) and methane hydrate destabilization (Kvenvolden, 1988; Archer, 2007). Human activity also contributes significantly to the total CH_4 emissions. Rice agriculture is one of the most important anthropogenic sources of CH_4 (Herrero et al., 2016; Schaefer et al., 2016). Other sources include landfills (Themelis and Ulloa, 2007), wastewater treatment, biomass burning, and methane slip from gas engines. Global fugitive CH_4 emissions from coal mining (Kort et al., 2014), natural gas and oil systems (Alvarez et al., 2018), hydraulic fracturing ("fracking") of shale gas wells (Howarth et al., 2011; Howarth, 2015, 2019), and residential and commercial natural gas distribution sectors (He et al., 2019) are also of increasing concern. Although the sources and sinks of methane are reasonably well known, there are large uncertainties in their relative amounts and in the partitioning between natural and anthropogenic contributions (Nisbet et al., 2014, 2016). This uncertainty is exemplified by the CH_4 "hiatus", which refers to the observed stabilization of atmospheric CH_4 concentrations from 1999–2006, and the renewed rise thereafter (Kirschke et al., 2013).

Satellite monitoring of CH_4 can be broadly divided into three categories: solar backscatter, thermal emission and lidar (Jacob et al., 2016). The first solar backscattering mission was SCIAMACHY (Frankenberg et al., 2006), which was operational from 2003–2012 and observed the entire planet once every seven days. It was followed by GOSAT in 2009 (Kuze et al., 2016), and subsequently the next generation GOSAT-2 in 2018 (Glumb et al., 2014). In between, the TROPOMI mission was also launched in 2017, which observes the planet once daily with a high spatial resolution of 7×7 km^2 (Butz

74   et al., 2012; Veefkind et al., 2012). CarbonSat (Buchwitz et al., 2013) is another proposed mission to

75   measure CH_4 globally from solar backscatter with a very fine spatial resolution (2×2 km^2) and high

76   precision (0.4%). Thermal infrared observations of CH_4 are available from the IMG (Clerbaux et al.,

77   2003), AIRS (Xiong et al., 2008), TES (Worden et al., 2012), IASI (Xiong et al., 2013), and CrIS

78   (Gambacorta et al., 2016) instruments. These instruments provide day/night measurements at spatial

79   resolutions ranging from 5×8 km^2 (TES) to 45×45 km^2 (AIRS). GEO-CAPE (Fishman et al., 2012),

80   GeoFTS (Xi et al., 2015), G3E (Butz et al., 2015), and GeoCarb (Polonsky et al., 2014) are proposed

81   geostationary instruments (GeoCarb was selected by NASA under the Earth Venture - Mission program),

82   which when operational will have resolutions of 2–5 km over regional scales. The MERLIN lidar

83   instrument (Kiemle et al., 2014) scheduled for launch in 2021 will measure CH_4 by employing a

84   differential absorption lidar.

85   By combining a large number of footprints and high spatial resolution, airborne imaging

86   spectrometers are also well suited for mapping local CH_4 plumes. The Airborne Visible/Infrared Imaging

87   Spectrometer–Next Generation (AVIRIS-NG) measures reflected solar radiance across more than 400

88   channels between 380 and 2500 nm (Green et al., 1998; Thompson et al., 2015). Strong CH_4 absorption

89   features present between 2100 and 2500 nm can be observed at a spectral resolution of 5 nm full width

90   at half maximum (FWHM). A number of approaches have been developed to retrieve CH_4 from such

91   hyperspectral data. Roberts et al. (2010) used a spectral residual approach between 2000 and 2500 nm

92   and Bradley et al. (2011) employed a band ratio technique using the 2298 nm CH_4 absorption band and

93   2058 nm CO_2 absorption band. However, these techniques are not suited for terrestrial locations that

94   have lower albedos and have spectral structure in the SWIR. A cluster-tuned matched filter technique

95   was demonstrated to be capable of mapping CH_4 plumes from marine and terrestrial sources (Thorpe et

96   al., 2013) as well as CO_2 from power plants (Dennison et al., 2013); however, this method does not

97   directly quantify gas concentrations. Frankenberg et al. (2005) developed an iterative maximum *a

98   posteriori* differential optical absorption spectroscopy (IMAP-DOAS) algorithm that allows for

99   uncertainty estimation. Thorpe et al. (2014) adapted the IMAP-DOAS algorithm for gas detection in

100 AVIRIS imagery. In addition, they developed a hybrid approach using singular value decomposition and

101 IMAP-DOAS as a complementary method of quantifying gas concentrations within complex AVIRIS

102 scenes.

103   Accurate assessment of CH_4 emissions is particularly challenging in the presence of aerosols

104 because the latter introduce uncertainties in the light path if not accounted for. In fact, CH_4 emissions are

105 frequently correlated with pollution due to concurrent aerosol emissions. For large aerosols (such as dust),

106 the low Ångström exponent values result in high aerosol optical depth (AOD) values even in the

107 wavelength range from 2000 nm to 2500 nm (Seinfeld and Pandis, 2006; Zhang et al., 2015). Therefore,

108 it is important to obtain a clear understanding of aerosol impacts on CH_4 retrievals. In this study, SWIR

109 AVIRIS-NG measurements are used to analyze the impact of aerosol scattering on CH_4 retrievals.

110 Further, using an accurate but numerically efficient radiative transfer (RT) model (Spurr and Natraj,

111 2011), we simulate AVIRIS-NG measurements with varying aerosol amounts and quantify the impact of

112 aerosol scattering using two retrieval techniques, the traditional matched filter (MF) method and the

113 optimal estimation (OE) method that is widely used in trace gas remote sensing. This article is organized

114 as follows. The MF and OE retrieval methods are described in Section 2. Section 3 focuses on analysis

115 of a sample CH_4 plume detected by AVIRIS-NG measurements and compares retrievals using the MF

116 and OE methods. Section 4 presents a detailed evaluation of aerosol impacts on the two retrieval methods

117 through simulations of AVIRIS-NG spectra for different geophysical parameters. Section 5 provides a

118 summary of the work and discusses future research.

119

120 **2 Methods**

121 **2.1 MF method**

122 Real-time remote detection using AVIRIS-NG measurements are traditionally based on the MF

123 method (Frankenberg et al., 2016). In this method, the background spectra are assumed to be distributed

124 as a multivariate Gaussian $\mathcal{N}$ with covariance matrix Σ and background mean radiance μ. If H_0 is a

125 scenario without CH_4 enhancement and H_1 is one with CH_4 enhancement, the MF approach is equivalent

126 to a hypothesis test between the two scenarios:

127
$$H_0: L_m \sim \mathcal{N}(\mu, \Sigma) \tag{1}$$

128
$$H_1: L_m \sim \mathcal{N}(\mu + t\alpha, \Sigma) \tag{2}$$

129 where L_m is the measurement radiance; t is the target signature, which is defined in Equation (4); α is the

130 enhancement value, denoting a scaling factor for the target signature that perturbs the background μ. If

131 x is a vector of measurement spectra with one element per wavelength, $\alpha(x)$ can be written, based on

132 maximum likelihood estimates (Manolakis et al., 2014), as follows:

133
$$\alpha(x) = \frac{(x - \mu)^T \Sigma^{-1} t}{t^T \Sigma^{-1} t} \tag{3}$$

134 We utilize the same definitions as in Frankenberg et al. (2016). Specifically, the enhancement value $\alpha(x)$

135 denotes the thickness and concentration within a volume of equivalent absorption, and has units of ppm

136 × m. The target signature t refers to the derivative of the change in measured radiance with respect to a

137 change in absorption path length due to an optically thin absorbing layer of CH_4. Note that this definition

138   has the disadvantage that the accuracy of the result degrades when the absorption is strong and further

139   attenuation becomes nonlinear. At a particular wavelength λ, t can be expressed as:

140
$$t(\lambda) = -\kappa(\lambda)\mu(\lambda), \tag{4}$$

141   where κ is the absorption coefficient for a near-surface plume with units of $ppm^{-1}\,m^{-1}$. This is

142   different from the units of $m^2 \cdot mol^{-1}$ traditionally used for the absorption coefficient κ_{trad} in trace

143   gas remote sensing. Using the ideal gas law to express the volume V (in liters) occupied by one mole of

144   CH_4 at the temperature and pressure corresponding to the plume altitude ($V = 22.4$ at standard

145   temperature and pressure), and the relations 1 liter $= 10^{-3}\,m^3$ and 1 ppm $= 10^{-6}$, we obtain the

146   following expression for unit conversion (units in parentheses):

147    $\kappa_{trad}\,[m^2 \cdot mol^{-1}] = \kappa\,[ppm^{-1}m^{-1}] \times V\,[liter\,mol^{-1}] \times 10^{-3}\,[m^3\,liter^{-1}] / 10^{-6}\,[ppm^{-1}]$(5)

148   Figure 1 shows the target signature, which is calculated based on HITRAN absorption cross-sections

149   (Rothman et al., 2009). The background mean radiance μ used in Equation 4 is based on the AVIRIS-

150   NG measurement shown in Figure 2; this is described in more detail in Section 3.

151   **2.2 OE method**

152   The OE method is widely used for the remote sensing retrieval of satellite measurements, such as

153   from the Orbiting Carbon Observatory-2 (OCO-2; O'Dell et al., 2018), the Spinning Enhanced Visible

154   and Infra-Red Imager (SEVIRI; Merchant et al., 2013), and the Greenhouse Gases Observing Satellite

155   (GOSAT; Yoshida et al., 2013). It combines an explicit (typically nonlinear) forward model of the

156   atmospheric state, a (typically Gaussian) prior probability distribution for the variabilities and a (typically

157   Gaussian) distribution for the spectral measurement errors. In addition, the Bayesian framework used by

158   the OE approach allows new information (from measurements) to be combined with existing information

159   (e.g., from models). In many applications, the forward model is nonlinear, and obtaining the optimal

160   solution requires iterative techniques such as the Levenberg–Marquardt method (Rodgers, 2000), which

161   has been routinely applied to study the impacts of measurement parameters on the retrieval process (see,

162   e.g., Zhang et al., 2015). The iteration in this algorithm follows the below procedure.

163
$$\mathbf{x_{i+1}} = \mathbf{x_i} + [(1+\gamma)\mathbf{S_a^{-1}} + \mathbf{K_i^T}\mathbf{S_\epsilon^{-1}}\mathbf{K_i}]^{-1}\{\mathbf{K_i^T}\mathbf{S_\epsilon^{-1}}[\mathbf{y} - \mathbf{F(x_i)}] - \mathbf{S_a^{-1}}[\mathbf{x_i} - \mathbf{x_a}]\} \tag{6}$$

164   where $\mathbf{x}$ is a state vector of surface and atmospheric properties, $\mathbf{S_a}$ is the *a priori* covariance matrix, $\mathbf{S_\epsilon}$

165   is the spectral radiance noise covariance matrix, $\mathbf{K}$ is the Jacobian matrix, $\mathbf{x_a}$ is the *a priori* state vector

166   and γ is a parameter determining the size of each iteration step. The measured spectral radiance is denoted

167   as $\mathbf{y}$; $\mathbf{F(x)}$ is the simulated radiance obtained from the forward model. For the retrieval of CH_4 from

168   AVIRIS-NG measurements, the state vector includes the total column amounts of CH_4 and H_2O, while

169   for the retrievals from synthetic spectra, the H_2O concentration is fixed and the state vector only includes

170   the CH_4 total column. The *a priori* values are within 10% of the true values; *a priori* errors are assumed

171 to be 20% for all state vector elements. The retrieved results are shown as the column averaged mixing

172 ratio (XCH$_4$, in ppm). Aerosols are not included in the state vector for both the real and synthetic

173 retrievals. They are, however, considered in the forward model for the synthetic simulations. Table 1

174 (WCRP, 1986) lists optical properties for four basic aerosol types (dust, water soluble, oceanic and soot).

175 Table 2 (WCRP, 1986) shows the corresponding properties for three aerosol models that are defined as

176 mixtures of the basic components from Table 1. We employ the Henyey-Greenstein phase function

177 (Henyey and Greenstein, 1941), where aerosol composition is determined by two parameters: single

178 scattering albedo (SSA) and asymmetry parameter (g). The surface albedo is also not retrieved; for both

179 real and synthetic retrievals, it is held fixed and assumed to be independent of wavelength.

180

181 **3 Detection and retrieval of CH$_4$ from AVIRIS-NG measurements**

182 To illustrate the OE retrieval and its difference from the MF method, we perform retrievals for an

183 AVIRIS-NG measurement made on 4 September 2014 (ang20140904t204546) in Bakersfield, CA, as

184 shown in Figure 2. The location is to the west of the Kern Front Oil field. This detection is a case study

185 from the NASA/ESA CO$_2$ and MEthane eXperiment (COMEX) campaign in California during June and

186 August/September 2014, which includes airborne *in situ*, airborne non-imaging remote sensing, and

187 ground-based *in situ* instruments to provide a real-time remote detection and measurement for CH$_4$

188 plumes released from anthropogenic sources. An RGB image of flight data is displayed in Figure 2a; the

189 emission source is a pump jack, as described in Thompson et al. (2015). Figure 2b presents results from

190 the MF method, which shows that the CH$_4$ plume disperses downwind and has a maximum enhancement

191 value of about 2800 ppm × m. Some artifacts caused by surfaces with strong absorption in the 2100–

192 2500 nm wavelength range, such as oil-based paints or roofs with calcite as a component (Thorpe et al.,

193 2013), also produce large α values in the MF method; these can be removed by an optimization method

194 such as the column-wise MF technique (Thompson et al., 2015).

195 Figure 3 displays the measured radiance (a) before normalization and (b) after normalization,

196 corresponding to two detector elements (in plume and out of plume). Every element is a cross-track

197 spatial location. The normalization is done by calculating the ratio of the radiance to the maximum value

198 across the spectral range, such that the values fall between 0 and 1. This is a first order correction for the

199 effects of surface albedo. Comparing the measured spectrum in plume to that out of plume, there is

200 obvious enhancement of CH$_4$ that is particularly evident in the normalized radiance. CH$_4$ is the main

201 absorber in the 2100–2500 nm wavelength range, and H$_2$O is the major interfering gas. Figure 3b

202 indicates the absorption peaks due to H$_2$O and CH$_4$.

203   We choose the plume center with 500 elements to illustrate results obtained using the MF and OE

204   methods. The former evaluates the CH_4 α value compared to the background CH_4 concentration, while

205   the latter retrieves XCH_4. In the MF method, the background covariance matrix Σ and mean radiance

206   μ are drawn from a reference region close to the CH_4 emission source. These are shown in Figure 2,

207   where the dashed green box denotes the reference region and the source is located within the solid red

208   box. In the OE method, results are shown as a multiplicative scaling factor compared to a typical XCH_4

209   background of 1.822 ppm. This value is the globally averaged marine surface annual mean for 2014 (Ed

210   Dlugokencky, NOAA/GML, www.esrl.noaa.gov/gmd/ccgg/trends_ch4/), the year corresponding to the

211   AVIRIS-NG measurement being studied. We use an accurate and numerically efficient two-stream-

212   exact-single-scattering (2S-ESS) RT model (Spurr and Natraj, 2011). This forward model is different

213   from a typical two-stream model in that the two-stream approximation is used only to calculate the

214   contribution of multiple scattering to the radiation field. Single scattering is treated in a numerically exact

215   manner using all moments of the phase function. This model has been used for remote sensing of

216   greenhouse gases and aerosols (Xi et al., 2015; Zhang et al., 2015, 2016; Zeng et al., 2017, 2018).

217   Aerosols are neither included in the forward model nor retrieved in this analysis. The surface albedo is

218   set to a wavelength-independent value of 0.5.

219   Results from the two retrieval methods reveal a similar CH_4 plume shape (Figure 4), especially for

220   elements with high CH_4 enhancement. However, larger differences in CH_4 concentrations are evident in

221   the OE retrievals (Figure 4b). Since radiance normalization reduces the impact of surface albedo and

222   aerosols are not included in either retrieval, this might be due to the fact that, in the OE method, H_2O and

223   CH_4 are simultaneously retrieved; the CH_4 retrieval has added uncertainty due to overlapping absorption

224   features between these two gases. The large maximum value of about 3000 in the MF method also

225   contributes to a reduction in relative contrast. While these results provide heuristic information about the

226   relative performance of the two retrieval techniques, it is difficult to compare the CH_4 enhancement

227   directly between the two methods since the background CH_4 concentration used in the MF method cannot

228   be quantified exactly. Further, evaluating retrieval biases due to ignoring aerosol scattering is not trivial

229   when real measurements are used. Therefore, we simulate synthetic spectra (see section 4) using the 2S-

230   ESS RT model to study the impacts of aerosol scattering as a function of different geophysical parameters

231   by varying them in a systematic manner.

232

233   **4 Aerosol impact analysis**

234   **4.1 Synthetic spectra**

235   In a real AVIRIS-NG observation, the exact column concentration of CH_4 cannot be controlled.

236   However, synthetic simulations allow us to manipulate parameters such as CH_4 concentration, surface

237   albedo, AOD, g, and SSA, and thereby test aerosol impacts on CH_4 retrievals. The 2S-ESS RT model is

238   used to simulate the AVIRIS-NG spectral radiance. In this model, a prior atmospheric profile with 70

239   layers from the surface up to 70 km is derived from National Center for Environmental Prediction

240   reanalysis data (Kalnay et al., 1996); absorption coefficients for all relevant gases are obtained from the

241   HITRAN database (Rothman et al., 2009). Monochromatic RT calculations are performed at a spectral

242   resolution of 0.5 cm^{-1}; the radiance spectrum is then convolved using a Gaussian instrument line shape

243   function with a wavelength-dependent full width at half maximum (FWHM) from a calibrated AVIRIS-

244   NG data file. The signal to noise ratio (SNR) is set to be 300, with Gaussian white noise added. This

245   procedure results in a wavelength grid with a resolution of about 5 nm. The spectral wavelength range

246   used to retrieve CH_4 is from 2100 nm to 2500 nm.

247   The additional atmospheric and geometric variables included in the model are listed in Table 3,

248   which are held constant unless otherwise mentioned. The observation geometry parameters are taken

249   from a real AVIRIS-NG measurement. Recent AVIRIS-NG fight campaigns have sensor heights ranging

250   from 0.43 to 3.8 km; we choose a value of 1 km, the same as the highest level where aerosol is present

251   in our simulations. The influence of AOD on CH_4 retrieval as a function of SSA and g is analyzed in

252   Section 4.3; in all other cases, SSA and g are held constant at 0.95 and 0.75, respectively, which is

253   representative of aerosols in the Los Angeles region (Zhang et al., 2015).

254   **4.2 Aerosol impact in the MF method**

255   We simulate synthetic spectra at different AOD, surface albedo and CH_4 concentration values, use

256   the MF method to obtain the CH_4 enhancement, and compare differences in α between scenarios without

257   and with aerosol. The covariance matrix and background mean radiance are calculated from a simulated

258   zero AOD background with surface albedos from 0.1 to 0.5, and XCH_4 set at the typical background

259   value of 1.822 ppm used in Section 3. Figure 5a shows the enhancement value as a function of XCH_4.

260   As the CH_4 concentration increases, the enhancement value obtained by the MF method at first increases

261   approximately linearly. However, the absorption changes in a nonlinear fashion with concentration,

262   whereas the MF method applies a linear formalism to the change. Therefore, the enhancement value

263   (which is correlated with the absorption signature) also shows a deviation from linear behavior at larger

264   XCH_4. Two aerosol scenarios (AOD = 0, 0.3) are compared in Figure 5a, which reveals that the effect of

265   aerosol loading is similar to an underestimation of CH_4 in the retrieval. The underestimation, which is

266   due to the shielding of CH_4 absorption below the aerosol layer and the fact that multiple scattering effects

267   between the aerosol and the surface are ignored, is clearly shown in Figure 5b, where the enhancement

268   value for fixed CH_4 concentration (same concentration as the background) decreases from 0 ppm × m

269   to −1532 ppm × m with increasing AOD. To clarify the impact of AOD at different surface albedo values,

270   zoomed in versions of α as a function of XCH_4 are presented in Figures 5c–f. For the AOD = 0 scenario,

271   the results are independent of surface albedo. This is because there are no multiple scattering effects

272   between the surface and the atmosphere (Rayleigh scattering is negligible in the retrieval wavelength

273   range) when there is no aerosol loading. For the scenarios with aerosol loading, the dispersion in the

274   zero-enhancement XCH_4 value between different surface albedos indicates that results from the MF

275   method are biased more at large AOD and surface albedo values (Figures 5d–f). This is a consequence

276   of increased multiple scattering between the aerosol layer and the surface that is not accounted for by the

277   retrieval algorithm. The maximum bias value is close to − 700 ppm × m (equivalent to − 0.06 × 1.822

278   ppm relative to the background concentration of 1.0 × 1.822 ppm) for an AOD of 0.3 and surface albedo

279   of 0.5 (Figure 5f). The implication of these results is that accurate knowledge of the surface albedo is

280   important for MF retrievals, especially when the aerosol loading is large.

281   A quantitative analysis of underestimation of CH_4 concentration due to aerosol scattering is

282   presented in Figure 6. The color bar shows the α bias — which is defined as the difference between the

283   enhancement value without aerosol (true α value) and that with aerosol — for different CH_4

284   concentrations, surface albedos and AODs. A positive bias means that CH_4 is underestimated. The α bias

285   increases with increasing surface albedo and AOD, reaching a maximum value of about 700 ppm × m

286   for the simulated cases. However, it is interesting that the bias decreases with increasing CH_4

287   concentration, which is different from the results obtained by the OE method (discussed in Section 4.3).

288   This surprising behavior is a direct consequence of the physical basis of the MF method. The rate of

289   increase in enhancement becomes smaller as XCH_4 becomes larger (Figure 5a). Therefore, at higher

290   XCH_4 values, the addition of aerosols (which has a similar effect as a reduction in XCH_4) results in a

291   lower reduction in enhancement compared to that at lower XCH_4 values, resulting in a net decrease in

292   the enhancement bias.

293   **4.3 Aerosol impact in the OE method**

294   For the simulation of the synthetic spectra, we assume nonzero aerosol loading below 1 km elevation.

295   The OE method is then used to perform retrievals using the same configuration (including, in particular,

296   the same surface albedo) except that AOD is set to zero. This approach is similar to neglecting aerosol

297   scattering in the CH_4 retrieval; the retrieval bias is defined as the difference between the true XCH_4 in

298   the simulation and the retrieved value (positive values refer to underestimation). First, we study the

299   retrieval bias caused by different aerosol types and mixtures. Figure 7a shows CH_4 retrieval biases as a

300   function of SSA and g; surface albedo and AOD are kept constant at 0.3 and XCH_4 is assumed to be 1.0

301 × 1.822 ppm. The retrieval bias increases with SSA and decreases with g, with a maximum bias ratio

302 (ratio of retrieval bias to the true value) of about 20%. This behavior can be explained as follows. At

303 higher SSA values, there are more multiple scattering effects (that are ignored in the retrieval). On the

304 other hand, larger values of g imply greater anisotropy of scattering (preference for forward scattering),

305 leading to a reduction in multiple scattering effects. Since the retrieval bias is large for high SSA and

306 low g, the water-soluble aerosol type (Table 1) and the maritime aerosol model (Table 2) can be expected

307 to induce greater biases in the retrieval. In order to compare the impacts of SSA and g in further detail,

308 retrieval results due to a ± 5% change in SSA and g for the three aerosol models from Table 2 are shown

309 in Figures 7b and 7c. Note that for the maritime aerosol model, the SSA is set to 0.999 for the +5%

310 scenario to ensure physicality. It is clear that (1) the maritime aerosol model induces larger retrieval

311 biases than the other aerosol types, and (2) the retrieval results are more sensitive to changes in g than

312 those in SSA.

313   We then simulate synthetic spectra for different values of CH_4 concentration, surface albedo and

314 AOD. The impacts of aerosol scattering on the retrievals for these scenarios are demonstrated in Figure

315 8. Figure 8a shows a 5 × 5 panel of boxes. Within each box, XCH_4 is constant, while surface albedo

316 increases from top to bottom and AOD increases from left to right. The variation of XCH_4 across the

317 boxes is shown in Figure 8b. We also show a zoomed in plot of the bottom right box ($XCH_4 = 5.8 \times$

318 1.822 ppm) in Figure 8c, which illustrates the AOD and surface albedo changes within a box. These

319 changes are identical for all boxes. Figure 8a indicates that OE retrievals produce larger CH_4 biases at

320 higher XCH_4 values, in contrast with MF results. In addition, it is evident that the retrieved CH_4 bias

321 increases with increasing AOD. The CH_4 bias induced by differences in the surface albedo is not as large

322 as that due to AOD variations, but surface albedo effects are noticeable at large AOD. Figure 8d shows

323 the sensitivity of retrieval biases to changes in AOD and surface albedo, again demonstrating the greater

324 impact of AOD than surface albedo in the retrieval.

325   The effects of changing the *a priori*, *a priori* error and RT simulation spectral resolution on the

326 retrieved XCH_4 are shown in Figure 9. For these calculations, the other parameters are set as follows:

327 SSA = 0.95, g = 0.75, AOD = 1.0, surface albedo = 0.5 and true XCH_4 = 5.8 × 1.822ppm. The parameters

328 were chosen to correspond to the scenario with the largest retrieval bias in Figure 8c (bottom right box

329 in Figure 8c). Figure 9a shows that the retrieved XCH_4 changes by about 9 ppb as the *a priori* changes

330 from half to twice the true XCH_4 value. Similarly, the XCH_4 difference is less than 4 ppb when the *a*

331 *priori* error changes from 0.05 to 0.5 (Figure 9b). Compared to the bias of about 923 ppb induced by

332 neglecting aerosol scattering for this scenario, it is clear that the impacts of the *a priori* and *a priori* error

333   are very small. The effect of spectral resolution is larger, but XCH_4 still changes by only about 100 ppb

334   when the spectral resolution is changed from 0.5 to 0.1 cm^{-1} (Figure 9c).

335   **4.4 Comparison of the two retrieval techniques**

336   Figure 10 presents the bias ratios for the two retrieval techniques at different AODs (surface albedo

337   = 0.3). In the MF method, the bias ratio is defined as the ratio of the bias to the true value of α. On the

338   other hand, in the OE method, it is the ratio of the bias to the true XCH_4. From Figure 10 it is clear that

339   the bias ratio decreases with increasing CH_4 concentration and has higher values at larger AODs. The

340   bias ratio for the MF method (1.3–4.5%) is up to 53.6% less than that for the OE method (2.8–5.6%) for

341   AOD = 0.3 when the CH_4 concentration is high (2–5 times typical background values). On the other

342   hand, the OE method performs better when enhancements are small and XCH_4 is close to the background

343   value. For example, the bias ratio for the MF method has a high value of about 42.6% at AOD = 0.3 for

344   a 10% enhancement ($XCH_4 = 1.1 \times 1.822$ ppm); the OE value for the same scenario is 8.6%. For scenarios

345   where scattering is ignored, the two retrieval techniques seem to be complementary, with differing

346   utilities for different enhancements. On the other hand, when RT models that account for scattering

347   effects are employed, the MF technique is suboptimal. Further, MF retrievals rely on accurate

348   characterization of the surface albedo, especially when the aerosol loading is large. Finally, the MF

349   method does not retrieve concentrations, which are necessary to infer fluxes. Therefore, the OE technique

350   is in general superior due to its ability to support simultaneous retrieval of aerosols, surface albedo and

351   CH_4 concentration.

352

353   **5 Summary and discussion**

354   Remote sensing measurements from airborne and satellite instruments are widely used to detect

355   CH_4 emissions. In our study, the traditional MF and the OE methods are used to quantify the effects of

356   aerosol scattering on CH_4 retrievals based on simulations of AVIRIS-NG measurements. The results

357   show that the retrieval biases increase with increasing AOD and surface albedo for both techniques. In

358   the OE method the biases increase with increasing CH_4 concentration and SSA, but decrease with

359   increasing aerosol asymmetry parameter. The CH_4 retrieval bias increases with increasing XCH_4 in the

360   OE method but decreases for the same scenario in the MF method. The surprising MF trend is attributed

361   to the inability of the MF method to treat nonlinear absorption effects at high XCH_4 values. We also

362   present bias ratios for the two techniques. The MF method shows smaller bias ratios at large CH_4

363   concentrations than the OE method; it is, therefore, the optimal method to detect strong CH_4 emission

364   sources when scattering effects can be ignored in the retrieval. For the same retrieval scenario, the OE

365   method seems to be more suitable for detecting diffuse sources. Further, the MF method relies on a

comparison with the background CH_4 concentration. It is difficult to get an accurate estimate of the background XCH_4 value in polluted atmospheric environments. In contrast, the OE method provides retrievals based solely on the atmospheric scenario of interest; CH_4, aerosols and surface albedo can be simultaneously inferred. Therefore, when scattering effects need to be considered, the OE method is the appropriate choice. Indeed, the MF method was intended for plume detection. OE enables accurate quantification of XCH_4 in the presence of aerosol scattering.

This study focused on a comparison of retrieval techniques. It is also important to accurately represent the physics of atmospheric RT, especially for scenarios with significant aerosol scattering. RT models traditionally used in retrievals of imaging spectroscopic data use simplified radiation schemes and predefined aerosol models, which may introduce inaccurate in the representation of atmospheric physics. The 2S-ESS model provides the capability to quantify aerosol impacts on CH_4 retrieval for different aerosol types, optical depths and layer heights. In future work, we will compare retrievals using the 2S-ESS model against those from other commonly used models such as MODTRAN. We will also evaluate the impact of varying instrument spectral resolution and signal to noise ratio for simultaneous retrieval of CH_4, surface albedo and AOD. This will be relevant for the design of imaging spectrometers for planned future missions such as the NASA Surface Biology and Geology (SBG) mission.

Acknowledgements

A portion of this research was carried out at the Jet Propulsion Laboratory, California Institute of Technology, under a contract with the National Aeronautics and Space Administration (80NM0018D0004). V.N. acknowledges support from the NASA "Utilization of Airborne Visible/Infrared Imaging Spectrometer Next Generation Data from an Airborne Campaign in India" program (solicitation NNH16ZDA001N-AVRSNG), and the Jet Propulsion Laboratory Research and Technology Development program. P.K. was funded by the Japan Society for the Promotion of Science International Research Fellow Program. The authors gratefully acknowledge the insightful and constructive comments from the two anonymous reviewers, which improved the clarity and quality of the manuscript, and elevated the significance of the work beyond the original expectation.

394 **References**

395

396 Alvarez, R. A., Zavala-Araiza, D., Lyon, D. R., Allen, D. T., Barkley, Z. R., Brandt, A. R., Davis, K. J.,

397 Herndon, S. C., Jacob, D. J., Karion, A., Kort, E. A., Lamb, B. K., Lauvaux, T., Maasakkers, J. D.,

398 Marchese, A. J., Omara, M., Pacala, S. W., Peischl, J., Robinson, A. L., Shepson, P. B., Sweeney, C.,

399 Townsend-Small, A., Wofsy, S. C., and Hamburg, S. P.: Assessment of methane emissions from the U.S.

400 oil and gas supply chain, Science, 361, 186–188, https://doi.org/10.1126/science.aar7204, 2018.

401

402 Archer, D.: Methane hydrate stability and anthropogenic climate change, Biogeosci., 4, 521–544,

403 https://doi.org/10.5194/bg-4-521-2007, 2007.

404

405 Bradley, E. S., Leifer, I., Roberts, D. A., Dennison, P. E., and Washburn, L.: Detection of marine methane

406 emissions with AVIRIS band ratios, Geophys. Res. Lett., 38, L10702,

407 https://doi.org/10.1029/2011GL046729, 2011.

408

409 Bubier, J. L., and Moore, T. R: An ecological perspective on methane emissions from northern wetlands,

410 Trends in Ecology and Evolution, 9, 460–464, https://doi.org/10.1016/0169-5347(94)90309-3, 1994.

411

412 Buchwitz, M., Reuter, M., Bovensmann, H., Pillai, D., Heymann, J., Schneising, O., Rozanov, V., Krings,

413 T., Burrows, J. P., Boesch, H., Gerbig, C., Meijer, Y., and Löscher, A.: Carbon Monitoring Satellite

414 (CarbonSat): Assessment of atmospheric CO_2 and CH_4 retrieval errors by error parameterization, Atmos.

415 Meas. Tech., 6, 3477–3500, https://doi.org/10.5194/amt-6-3477-2013, 2013.

416

417 Butz, A., Galli, A., Hasekamp, O., Landgraf, J., Tol, P., and Aben, I.: TROPOMI aboard Sentinel-5

418 Precursor: Prospective performance of CH_4 retrievals for aerosol and cirrus loaded atmospheres, Remote

419 Sens. Environ., 120, 267–276, https://doi.org/10.1016/j.rse.2011.05.030, 2012.

420

421 Butz, A., Orphal, J., Checa-Garcia, R., Friedl-Vallon, F., von Clarmann, T., Bovensmann, H., Hasekamp,

422 O., Landgraf, J., Knigge, T., Weise, D., Sqalli-Houssini, O., and Kemper, D.: Geostationary Emission

423 Explorer for Europe (G3E): Mission concept and initial performance assessment, Atmos. Meas. Tech., 8,

424 4719–4734, https://doi.org/10.5194/amt-8-4719-2015, 2015.

425

426   Clerbaux, C., Hadji-Lazaro, J., Turquety, S., Mégie, G., and Coheur, P.-F.: Trace gas measurements from

427   infrared satellite for chemistry and climate applications, Atmos. Chem. Phys., 3, 1495–1508,

428   https://doi.org/10.5194/acp-3-1495-2003, 2003.

429

430   Dennison, P. E., Thorpe, A. K., Pardyjak, E. R., Roberts, D. A., Qi, Y., Green, R. O., Bradley, E. S., and

431   Funk, C. C.: High spatial resolution mapping of elevated atmospheric carbon dioxide using airborne

432   imaging spectroscopy: Radiative transfer modeling and power plant plume detection, Remote Sens.

433   Environ., 139, 116-129, https://doi.org/10.1016/j.rse.2013.08.001, 2013.

434

435   Etiope, G., Feyzullayev, A., and Baciu, C. L.: Terrestrial methane seeps and mud volcanoes: A global

436   perspective of gas origin, Mar. Pet. Geol., 26, 333–344, https://doi.org/10.1016/j.marpetgeo.2008.03.001,

437   2009.

438

439   Fishman, J. L., Iraci, L. T., Al-Saadi, J., Chance, K., Chavez, F., Chin, M., Coble, P., Davis, C.,

440   DiGiacomo, P. M., Edwards, D., Eldering, A., Goes, J., Herman, J., Hu, C., Jacob, D. J., Jordan, C., Kawa,

441   S. R., Key, R., Liu, X., Lohrenz, S., Mannino, A., Natraj, V., Neil, D., Neu, J., Newchurch, M., Pickering,

442   K., Salisbury, J., Sosik, H., Subramaniam, A., Tzortziou, M.,Wang, J., and Wang, M.: The United States'

443   next generation of atmospheric composition and coastal ecosystem measurements: NASA's

444   Geostationary Coastal and Air Pollution Events (GEO-CAPE) Mission, Bull. Am. Meteorol. Soc.,

445   https://doi.org/10.1175/BAMS-D-11-00201.1, 2012.

446

447   Frankenberg, C., Platt, U., and Wagner, T.: Iterative maximum a posteriori (IMAP)-DOAS for retrieval

448   of strongly absorbing trace gases: Model studies for CH_4 and CO_2 retrieval from near infrared spectra of

449   SCIAMACHY onboard ENVISAT, Atmos. Chem. Phys., 5, 9–22, https://doi.org/10.5194/acp-5-9-2005,

450   2005.

451

452   Frankenberg, C., Meirink, J. F., Bergamaschi, P., Goede, A., P. H., Heimann, M., Körner, S., Platt, U.,

453   van Weele, M., and Wagner, T.: Satellite chartography of atmospheric methane from SCIAMACHY on

454   board ENVISAT: Analysis of the years 2003 and 2004, J. Geophys. Res., 111, D07303,

455   https://doi.org/10.1029/2005JD006235, 2006.

456

457   Frankenberg, C., Thorpe, A. K., Thompson, D. R., Hulley, G., Kort, E. A., Vance, N., Borchardt, J.,

458   Krings, T., Gerilowski, K., Sweeney, C., Conley, S., Bue, B. D., Aubrey, A. D., Hook, S., and Green, R.

459 O.: Airborne methane remote measurements reveal heavy-tail flux distribution in Four Corners region,

460 Proc. Natl. Acad. Sci. U. S. A., 113, 9734–9739, https://doi.org/10.1073/pnas.1605617113, 2016.

461

462 Gambacorta, A., Barnet, C. D., Smith, N., Pierce, R. B., Smith, J. W., Spackman, J. R., and Goldberg,

463 M.: The NPP and J1 NOAA Unique Combined Atmospheric Processing System (NUCAPS) for

464 atmospheric thermal sounding: Recent algorithm enhancements tailored to near real time users

465 applications, Abstract IN33D-07, presented at 2016 Fall Meeting, AGU, San Francisco, CA, 12–16 Dec.,

466 2016.

467

468 Gedney, N., Cox, P. M., and Huntingford, C.: Climate feedback from wetland methane emissions,

469 Geophys. Res. Lett., 31, L20503. https://doi.org/10.1029/2004GL020919, 2004.

470

471 Glumb, R., Davis, G., and Lietzke, C.: The TANSO-FTS-2 instrument for the GOSAT-2 greenhouse gas

472 monitoring mission, 2014 IEEE Geoscience and Remote Sensing Symposium, Quebec City, QC, 1238–

473 1240, https://doi.org/10.1109/IGARSS.2014.6946656, 2014.

474

475 Green, R. O., Eastwood, M. L., Sarture, C. M., Chrien, T. G., Aronsson, M., Chippendale, B. J., Faust,

476 J. A., Pavri, B. E., Chovit, C. J., Solis, M., Olah, M. R., and Williams, O.: Imaging spectroscopy and the

477 Airborne Visible/Infrared Imaging Spectrometer (AVIRIS), Remote Sens. Environ., 65, 227–248,

478 https://doi.org/10.1016/S0034-4257(98)00064-9, 1998.

479

480 He, L., Zeng, Z.-C., Pongetti, T. J., Wong, C., Liang, J., Gurney, K. R., Newman, S., Yadav, V., Verhulst,

481 K., Miller, C. E., and Duren, R.: Atmospheric methane emissions correlate with natural gas consumption

482 from residential and commercial sectors in Los Angeles, Geophys. Res. Lett., 46, 8563–8571,

483 https://doi.org/10.1029/2019GL083400, 2019.

484

485 Henyey, L. G., and Greenstein, J. L.: Diffuse radiation in the galaxy, Astrophys. J., 93, 70–83,

486 https://doi.org/10.1086/144246, 1941.

487

488 Herrero, M., Henderson, B., Havlík, P., Thornton, P. K., Conant, R. T., Smith, P., Wirsenius, S., Hristov,

489 A. N., Gerber, P., Gill, M., Butterbach-Bahl, K., Valin, H., Garnett, T., and Shehfest, E.: Greenhouse gas

490 mitigation potentials in the livestock sector, Nature Clim. Change, 6, 452–461,

491 https://doi.org/10.1038/nclimate2925, 2016.

Holmes, C. D., Prather, M. J., Søvde, O. A., and Myhre, G.: Future methane, hydroxyl, and their uncertainties: key climate and emission parameters for future predictions, Atmos. Chem. Phys., 13, 285–302, https://doi.org/10.5194/acp-13-285-2013, 2013.

Howarth, R. W.: Methane emissions and climatic warming risk from hydraulic fracturing and shale gas development: implications for policy, Energy and Emission Control Technologies, 3, 45–54, https://doi.org/10.2147/EECT.S61539, 2015.

Howarth, R. W.: Ideas and perspectives: is shale gas a major driver of recent increase in global atmospheric methane?, Biogeosciences, 16, 3033–3046, https://doi.org/10.5194/bg-16-3033-2019, 2019.

Howarth, R. W., Santoro, R., and Ingraffea, A.: Methane and the greenhouse gas footprint of natural gas from shale formations, Clim. Change, 106, 679, https://doi.org/10.1007/s10584-011-0061-5, 2011.

Jacob, D. J., Turner, A. J., Maasakkers, J. D., Sheng, J., Sun, K., Liu, X., Chance, K., Aben, I., McKeever, J., and Frankenberg, C.: Satellite observations of atmospheric methane and their value for quantifying methane emissions, Atmos. Chem. Phys., 16, 14371–14396, https://doi.org/10.5194/acp-16-14371-2016, 2016.

Kalnay, E., Kanamitsu, M., Kistler, R., Collins, W., Deaven, D., Gandin, L., Iredell, M., Saha, S., White, G., Woollen, J., Zhu, Y., Chelliah, M., Ebisuzaki, W., Higgins, W., Janowiak, J., Mo, K. C., Ropelewski, C., Wang, J., Leetmaa, A., Reynolds, R., Jenne, R., and Joseph, D.: The NCEP/NCAR 40-year reanalysis project, Bull. Am. Meteorol. Soc., 77, 437–471, https://doi.org/10.1175/1520-0477(1996)077<0437:TNYRP>2.0.CO;2, 1996.

Kiemle, C., Kawa, S. R., Quatrevalet, M., and Browell, E. V.: Performance simulations for a spaceborne methane lidar mission, J. Geophys. Res., 119, 4365–4379, https://doi.org/10.1002/2013JD021253, 2014.

Kirschke, S., Bousquet, P., Ciais, P., Saunois, M., Canadell, Josep G., Dlugokencky. E. J., Bergamaschi, P., Bergmann, D., Blake, D. R., Bruhwiler, L., Cameron-Smith, P., Castaldi, S., Chevallier, F., Feng, L., Fraser, A., Heimann, M, Hodson, E. L., Houweling, S., Josse, B., Fraser, P. J., Krummel, P. B., Lamarque, J.-F., Langenfelds, R. L., Le Quere, C., Naik, V., O'Doherty, S., Palmer, P. I., Pison, I., Plummer, D., Poulter, B., Prinn, R. G., Rigby, M., Ringeval, B., Santini, M. Schmidt, M., Shindell, D. T., Simpson, I.

525   J., Spahni, R., Steele, L. P., Strode, S. A., Sudo, K., Szopa, S., van der Werf, G. R., Voulgarakis, A., van

526   Weele, M., Weiss, R. F., Williams, J. E., and Zeng, G.: Three decades of global methane sources and

527   sinks, Nature Geosci., 6, 813–823, https://doi.org/10.1038/ngeo1955, 2013.

528

529   Kort, E. A., Frankenberg, C., Costigan, K. R., Lindenmaier, R., Dubey, M. K., and Wunch, D.: Four

530   corners: the largest US methane anomaly viewed from space, Geophys. Res. Lett., 41, 6898–6903,

531   https://doi.org/10.1002/2014GL061503, 2014.

532

533   Kuze, A., Suto, H., Shiomi, K., Kawakami, S., Tanaka, M., Ueda, Y., Deguchi, A., Yoshida, J., Yamamoto,

534   Y., Kataoka, F., Taylor, T. E., and Buijs, H. L.: Update on GOSAT TANSO-FTS performance, operations,

535   and data products after more than 6 years in space, Atmos. Meas. Tech., 9, 2445–2461,

536   https://doi.org/10.5194/amt-9-2445-2016, 2016.

537

538   Kvenvolden, K. A.: Methane hydrate – A major reservoir of carbon in the shallow geosphere, Chem.

539   Geol., 71, 41–51, https://doi.org/10.1016/0009-2541(88)90104-0, 1988.

540

541   Kvenvolden, K. A., and Rogers, B. W.: Gaia's breath – global methane exhalations, Mar. Pet. Geol., 22,

542   579–590, https://doi.org/10.1016/j.marpetgeo.2004.08.004, 2005.

543

544   Macdonald, J. A., Fowler, D., Hargreaves, K. J., Skiba, U., Leith, I. D., and Murray, M. B.: Methane

545   emission rates from a northern wetland; response to temperature, water table and transport, Atmos.

546   Environ., 32, 3219–3227, https://doi.org/10.1016/S1352-2310(97)00464-0, 1998.

547

548   Manolakis, D., Truslow, E., Pieper, M., Cooley, T., and Brueggeman, M.: Detection algorithms in

549   hyperspectral imaging systems: An overview of practical algorithms, IEEE Signal Proc. Mag., 31, 24–

550   33, https://doi.org/10.1109/MSP.2013.2278915, 2014.

551

552   Merchant, C. J., Le Borgne, P., Roquet, H., and Legendre, G.: Extended optimal estimation techniques

553   for sea surface temperature from the Spinning Enhanced Visible and Infra-Red Imager (SEVIRI),

554   Remote Sens. Environ., 131, 287–297, https://doi.org/10.1016/j.rse.2012.12.019, 2013.

555

556   Myhre, G., Shindell, D., Bréon, F.-M., Collins, W., Fuglestvedt, J., Huang, J., Koch, D., Lamarque, J.-

557   F., Lee, D., Mendoza, B., Nakajima, T., Robock, A., Stephens, G., Takemura, T., and Zhang, H.:

558   Anthropogenic and Natural Radiative Forcing, Climate Change 2013: The Physical Science Basis.

559   Contribution of Working Group I to the Fifth Assessment Report of the Intergovernmental Panel on

560   Climate Change – IPCC, 2013.

561

562   Nisbet, E. G., Dlugokencky, E, J., and Bousquet, P.: Methane on the rise-Again, Science, 343, 493–495,

563   https//doi.org/10.1126/science.1247828, 2014.

564

565   Nisbet, E. G., Dlugokencky, E. J., Manning, M. R., Lowry, D., Fisher, R. E., France, J. L., Michel, S. E.,

566   Miller, J. B., White, J. W. C., Vaughn, B., Bousquet, P., Pyle, J. A., Warwick, N. J., Cain, M., Brownlow,

567   R., Zazzeri, G., Lanoisellé, M., Manning, A. C., Gloor, E., Worthy, D. E. J., Brunke, E.-G., Labuschagne,

568   C., Wolff, E. W., and Ganesan, A. L.: Rising atmospheric methane: 2007–2014 growth and isotopic shift,

569   Glob. Biogeochem. Cycles, 30, 1356–1370, https://doi.org/10.1002/2016GB005406, 2016.

570

571   NOAA   Earth   System   Research   Laboratory   Global   Monitoring   Laboratory,

572   https://esrl.noaa.gov/gmd/ccgg/trends_ch4/, 2019.

573

574   O'Dell, C. W., Eldering, A., Wennberg, P. O., Crisp, D., Gunson, M. R., Fisher, B., Frankenberg, C.,

575   Kiel, M., Lindqvist, H., Mandrake, L., Merrelli, A., Natraj, V., Nelson, R. R., Osterman, G. B., Payne,

576   V. H., Taylor, T. E., Wunch, D., Drouin, B. J., Oyafuso, F., Chang, A., McDuffie, J., Smyth, M., Baker,

577   D. F., Basu, S., Chevallier, F., Crowell, S. M. R., Feng, L., Palmer, P. I., Dubey, M., García, O. E.,

578   Griffith, D. W. T., Hase, F., Iraci, L. T., Kivi, R., Morino, I., Notholt, J., Ohyama, H., Petri, C., Roehl,

579   C. M., Sha, M. K., Strong, K., Sussmann, R., Te, Y., Uchino, O. and Velazco, V. A.: Improved retrievals

580   of carbon dioxide from Orbiting Carbon Observatory-2 with the version 8 ACOS algorithm, Atmos.

581   Meas. Tech., 11(12), 6539–6576, https://doi.org/10.5194/amt-11-6539-2018, 2018.

582

583   Polonsky, I. N., O'Brien, D. M., Kumer, J. B., O'Dell, C. W., and the geoCARB Team: Performance of

584   a geostationary mission, geoCARB, to measure CO_2, CH_4 and CO column-averaged concentrations,

585   Atmos. Meas. Tech., 7, 959–981, https://doi.org/10.5194/amt-7-959-2014, 2014.

586

587   Roberts, D. A., Bradley, E. S., Cheung, R., Leifer, I., Dennison, P. E., and Margolis, J. S.: Mapping

588   methane emissions from a marine geological seep source using imaging spectrometry, Remote Sens.

589   Environ., 114, 592–606, https://doi.org/10.1016/j.rse.2009.10.015, 2010.

590

591 Rodgers, C. D.: Inverse Methods for Atmospheric Sounding: Theory and Practice, World Scientific,

592 Singapore, 2000.

593

594 Rothman, L. S., Gordon, I. E., Barbe, A., Benner, D. C., Bernath, P. E., Birk, M., Boudon, V., Brown,

595 L. R., Campargue, A., Champion, J. P., Chance, K., Coudert, L. H., Dana, V., Devi, V. M., Fally, S.,

596 Flaud, J. M., Gamache, R. R., Goldman, A., Jacquemart, D., Kleiner, I., Lacome, N., Lafferty, W. J.,

597 Mandin, J. Y., Massie, S. T., Mikhailenko, S. N., Miller, C. E., Moazzen-Ahmadi, N., Naumenko, O. V.,

598 Nikitin, A. V., Orphal, J., Perevalov, V. I., Perrin, A., Predoi-Cross, A., Rinsland, C. P., Rotger, M.,

599 Šimečková, M., Smith, M. A. H., Sung, K., Tashkun, S. A., Tennyson, J., Toth, R. A., Vandaele, A. C.,

600 and Vander Auwera, J.: The HITRAN 2008 molecular spectroscopic database, J. Quant. Spectrosc.

601 Radiat. Transfer, 110, 533–572, https://doi.org/10.1016/j.jqsrt.2009.02.013, 2009.

602

603 Schaefer, H., Fletcher, S. E. M., Veidt, C., Lassey, K. R., Brailsford, G. W., Bromley, T. M.,

604 Dlugokencky, E. J., Michel, S. E., Miller, J. M., Levin, I., Lowe, D. C., Martin, R. J., Vaughn, B. H., and

605 White, J. W. C.: A 21st-century shift from fossil-fuel to biogenic methane emissions indicated by $^{13}CH_4$,

606 Science, 352, 80-84, https://doi.org/10.1126/science.aad2705, 2016.

607

608 Schaefer, K., Lantuit, H., Romanovsky, V. E., Schuur, E. A. G., and Witt, R.: The impact of the

609 permafrost carbon feedback on global climate, Environ. Res. Lett., 9, 085003,

610 https://doi.org/10.1088/1748-9326/9/8/085003, 2014.

611

612 Schuur, E. A. G., McGuire, A. D., Schädel, C., Grosse, G., Harden, J. W., Hayes, D. J., Hugelius, G.,

613 Koven, C. D., Kuhry, P., Lawrence, D. M., Natali, S. M., Olefeldt, D., Romanovsky, V. E., Schaefer, K.,

614 Turetsky, M. R., Treat, C. C., and Vonk, J. E.: Climate change and the permafrost carbon feedback,

615 Nature, 520, 171–179, https://doi.org/10.1038/nature14338, 2015.

616

617 Seinfeld, J. H., and Pandis, S. N.: Atmospheric Chemistry and Physics: From Air Pollution to Climate

618 Change, Wiley, New Jersey, USA, 2006.

619

620 Spurr, R., and Natraj, V.: A linearized two-stream radiative transfer code for fast approximation of

621 multiple-scatter fields, J. Quant. Spectrosc. Radiat. Transfer, 112, 2630–2637,

622 https://doi.org/10.1016/j.jqsrt.2011.06.014, 2011.

623

624   Themelis, N. J., and Ulloa, P. A.: Methane generation in landfills, Renewable Energy, 32, 1243–1257,

625   https://doi.org/10.1016/j.renene.2006.04.020, 2007.

626

627   Thompson, D. R., Leifer, I., Bovensmann, H., Eastwood, M., Fladeland, M., Frankenberg, C.,

628   Gerilowski, K., Green, R. O., Kratwurst, S., Krings, T., Luna, B., and Thorpe, A. K.: Real-time remote

629   detection and measurement for airborne imaging spectroscopy: a case study with methane, Atmos. Meas.

630   Tech., 8, 4383–4397, https://doi.org/10.5194/amt-8-4383-2015, 2015.

631

632   Thorpe, A. K., Frankenberg, C., and Roberts, D. A.: Retrieval techniques for airborne imaging of

633   methane concentrations using high spatial and moderate spectral resolution: Application to AVIRIS,

634   Atmos. Meas. Tech., 7, 491–506, https://doi.org/10.5194/amt-7-491-2014, 2014.

635

636   Thorpe, A. K., Roberts, D. A., Bradley, E. S., Funk, C. C., Dennison, P. E., and Leifer, I.: High resolution

637   mapping of methane emissions from marine and terrestrial sources using a Cluster-Tuned Matched Filter

638   technique and imaging spectrometry, Remote Sens. Environ., 134, 305–318,

639   https://doi.org/10.1016/j.rse.2013.03.018, 2013.

640

641   Veefkind, J. P., Aben, I., McMullan, K., Forster, H., de Vries, J.,Otter, G., Claas, J., Eskes, H. J., de Haan,

642   J. F., Kleipool, Q., van Weele, M., Hasekamp, O., Hoogeveen, R., Landgraf, J., Snel, R., Tol, P., Ingmann,

643   P., Voors, R., Kruizinga, B., Vink, R., Visser, H., and Levelt, P. F.: TROPOMI on the ESA Sentinel-5

644   Precursor: A GMES mission for global observations of the atmospheric composition for climate, air

645   quality and ozone layer applications, Remote Sens. Environ., 120, 70–83,

646   https://doi.org/10.1016/j.rse.2011.09.027, 2012.

647

648   Walter, K. M., Zimov, S. A., Chanton, J. P., Verbyla, D., and Chapin III, F. S.: Methane bubbling from

649   Siberian thaw lakes as a positive feedback to climate warming, Nature, 443, 71–75,

650   https://doi.org/10.1038/nature05040, 2006.

651

652   World Climate Research Program (WCRP): A preliminary cloudless standard atmosphere for radiation

653   computation, International Association for Meteorology and Atmospheric Physics, Radiation

654   Commission, Boulder, CO, USA, 1984, CSP-112, WMO/TD-No. 24, March 1986.

655

656 Woodwell, G. M., Mackenzie, F. T., Houghton, R. A., Apps, M., Gorham, E., and Davidson, E.: Biotic
657 feedbacks in the warming of the earth, Climatic Change, 40, 495–518,
658 https://doi.org/10.1023/A:1005345429236, 1998.

660 Worden, J., Kulawik, S., Frankenberg, C., Payne, V., Bowman, K., Cady-Peirara, K., Wecht, K., Lee, J.-
661 E., and Noone, D.: Profiles of CH_4, HDO, H_2O, and N_2O with improved lower tropospheric vertical
662 resolution from Aura TES radiances, Atmos. Meas. Tech., 5, 397–411, https://doi.org/10.5194/amt-5-
663 397-2012, 2012.

665 Xi, X., Natraj, V., Shia, R. L., Luo, M., Zhang, Q., Newman, S., Sander, S. P., and Yung, Y. L.: Simulated
666 retrievals for the remote sensing of CO_2, CH_4, CO, and H_2O from geostationary orbit, Atmos. Meas.
667 Tech., 8, 4817–4830, https://doi.org/10.5194/amtd-8-5809-2015, 2015.

669 Xiong, X., Barnet, C., Maddy, E., Sweeney, C., Liu, X., Zhou, L., and Goldberg, M.: Characterization
670 and validation of methane products from the Atmospheric Infrared Sounder (AIRS), J. Geophys. Res.,
671 113, G00A01, https://doi.org/10.1029/2007JG000500, 2008.

673 Xiong, X., Barnet, C., Maddy, E. S., Gambacorta, A., King, T. S., and Wofsy, S. C.: Mid-upper
674 tropospheric methane retrieval from IASI and its validation, Atmos. Meas. Tech., 6, 2255–2265,
675 https://doi.org/10.5194/amt-6-2255-2013, 2013.

677 Yoshida, Y., Kikuchi, N., Morino, I., Uchino, O., Oshchepkov, S., Bril, A., Saeki, T., Schutgens, N.,
678 Toon, G. C., Wunch, D., Roehl, C. M., Wennberg, P. O., Griffith, D. W. T., Deutscher, N. M., Warneke,
679 T., Notholt, J., Robinson, J., Sherlock, V., Connor, B., Rettinger, M., Sussmann, R., Ahonen, P.,
680 Heikkinen, P., Kyrö, E., Mendonca, J., Strong, K., Hase, F., Dohe, S., and Yokota, T.: Improvement of
681 the retrieval algorithm for GOSAT SWIR XCO_2 and XCH_4 and their validation using TCCON data,
682 Atmos. Meas. Tech., 6, 1533–1547, https://doi.org/10.5194/amt-6-1533-2013, 2013.

684 Zeng, Z.-C., Zhang, Q., Natraj, V., Margolis, J. S., Shia, R. -L., Newman, S., Fu, D., Pongetti, T. J.,
685 Wong, K. W., Sander, S. P., Wennberg, P. O., and Yung, Y. L.: Aerosol scattering effects on water vapor
686 retrievals over the Los Angeles Basin, Atmos. Chem. Phys., 17, 2495–2508, https://doi.org/10.5194/acp-
687 17-2495-2017, 2017.

689   Zeng, Z.-C., Natraj, V., Xu, F., Pongetti, T. J., Shia, R.-L., Kort, E. A., Toon, G. C., Sander, S. P., and

690   Yung, Y. L.: Constraining aerosol vertical profile in the boundary layer using hyperspectral

691   measurements of oxygen absorption, Geophys. Res. Lett., 45, 10772–10780,

692   https://doi.org/10.1029/2018GL079286, 2018.

693

694   Zhang, Q., Natraj, V., Li, K. -F., Shia, R. -L., Fu, D., Pongetti, T. J., Sander S. P., Roehl, C. M., and

695   Yung, Y. L.: Accounting for aerosol scattering in the CLARS retrieval of column averaged CO_2 mixing

696   ratios, J. Geophys. Res., 120, 7205–7218, https://doi.org/10.1002/2015JD023499, 2015.

697

698   Zhang, Q., Shia, R. -L., Sander, S. P., and Yung, Y. L.: X_{CO2} retrieval error over deserts near critical

699   surface albedo, Earth Space Sci., 2, 1–10, https://doi.org/10.1002/2015EA000143, 2016.

700

701
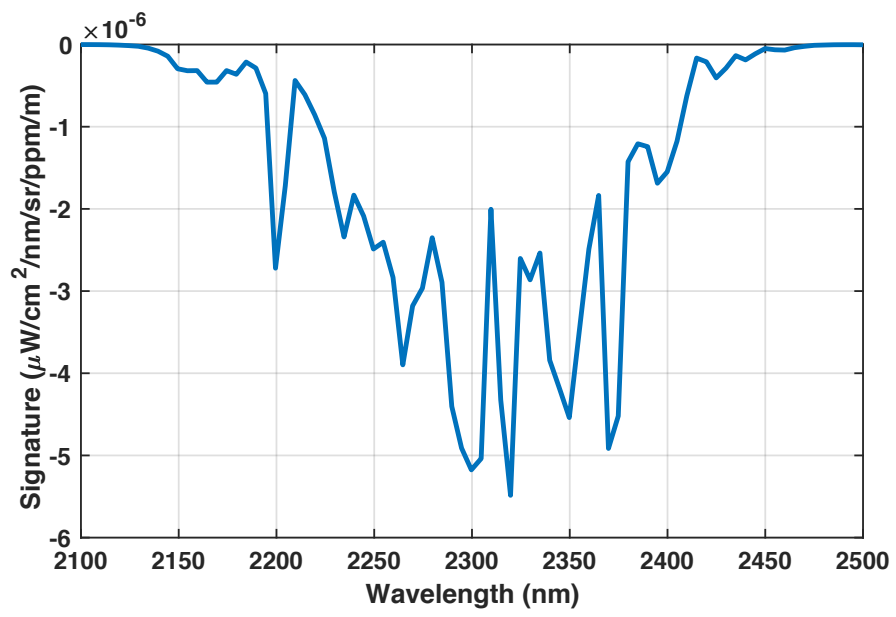
702

703

704   **Figure 1: The target signature used for the Matched Filter method.**

705

706

707
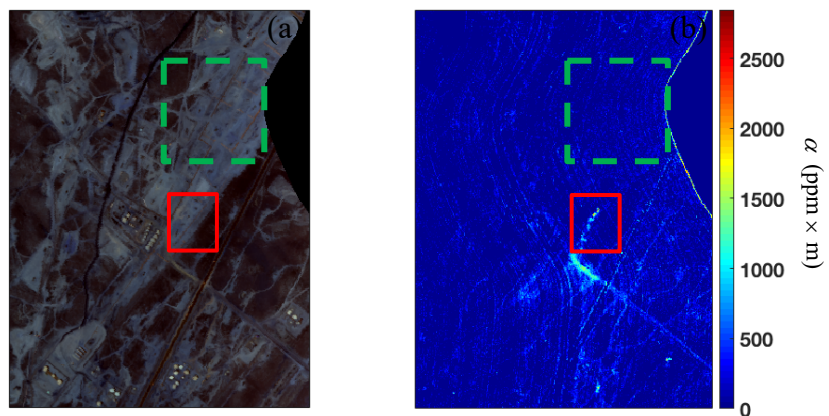
Figure 2: (a) RGB image of flight data from 4 September 2014 (ang20140904t204546). Adapted from Thompson et al. (2015). (b) CH$_4$ enhancement value α (ppm × m) obtained by the MF method. An emission source is shown in the solid red box and the background region near the target for the MF calculation is indicated by the dashed green box.

712

713
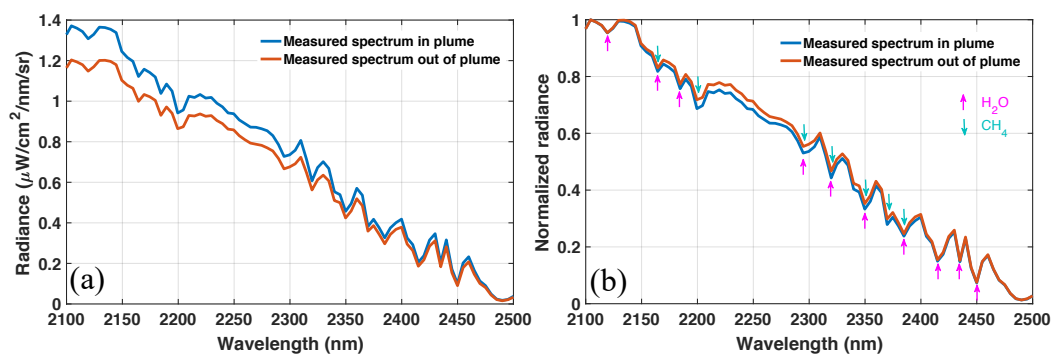
714

715 **Figure 3: (a) Real radiance and (b) normalized radiance at cross-track detector elements (in and out of plume)**

716 **from the sample AVIRIS-NG measurement. The colored arrows in (b) show the main absorption features due**

717 **to H_2O (purple) and CH_4 (green).**

718

719
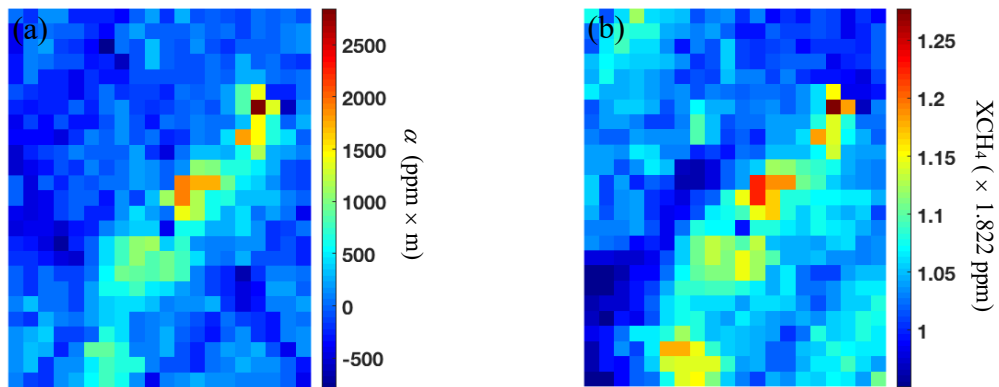
720

721 **Figure 4: Retrieval image for the plume center (500 elements) based on the (a) MF method and (b) OE method.**

722

723

724
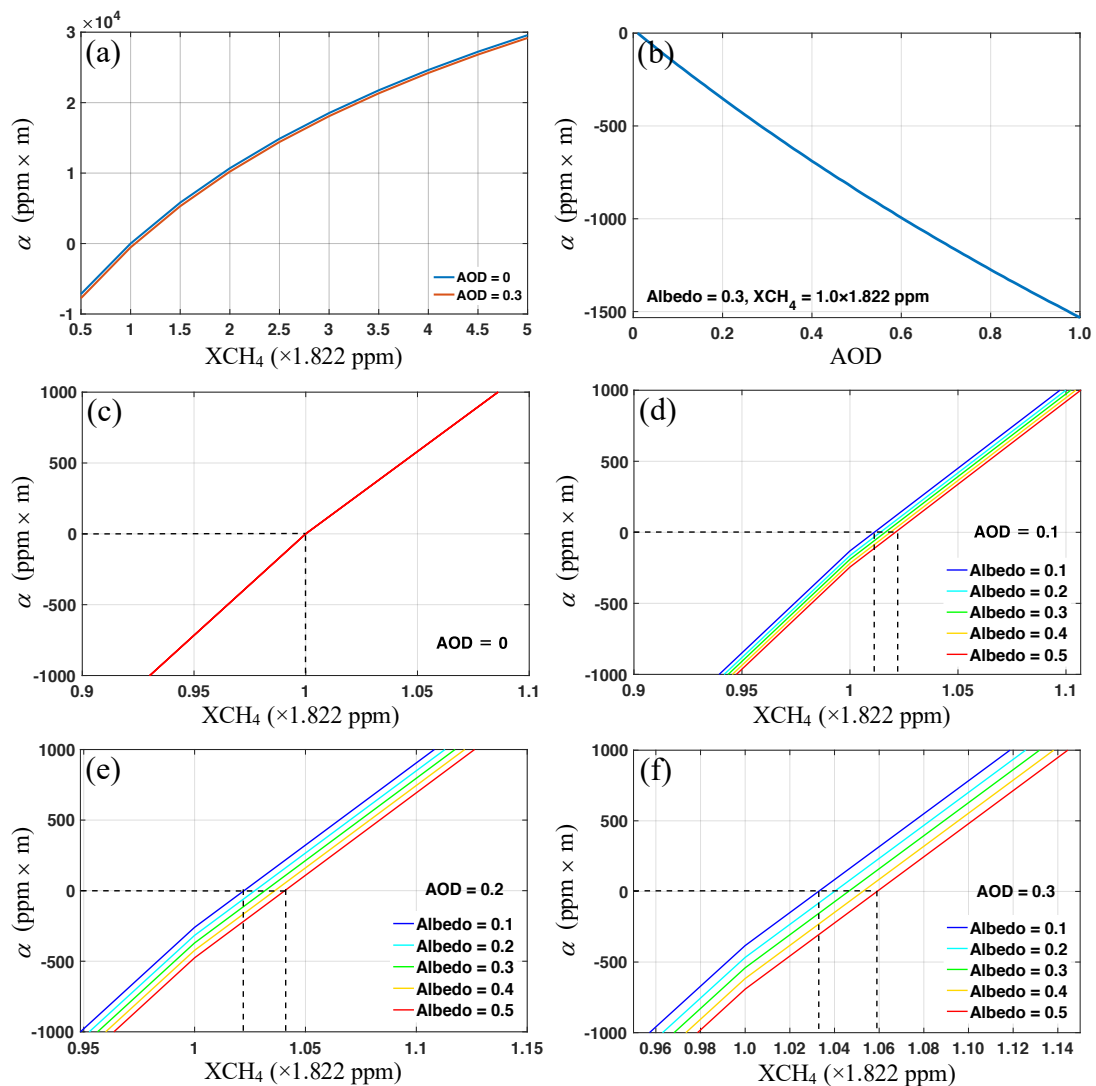
Figure 5: (a) α as a function of XCH$_4$ for AOD = 0 and AOD = 0.3 (surface albedo = 0.3). (b) α as a function of AOD (XCH$_4$ = 1.0 × 1.822 ppm, surface albedo = 0.3). Zoomed in versions of α as a function of XCH$_4$ for different surface albedos (0.1-0.5), where (c) AOD = 0, (d) AOD = 0.1, (e) AOD = 0.2, and (f) AOD = 0.3.

728

729

730
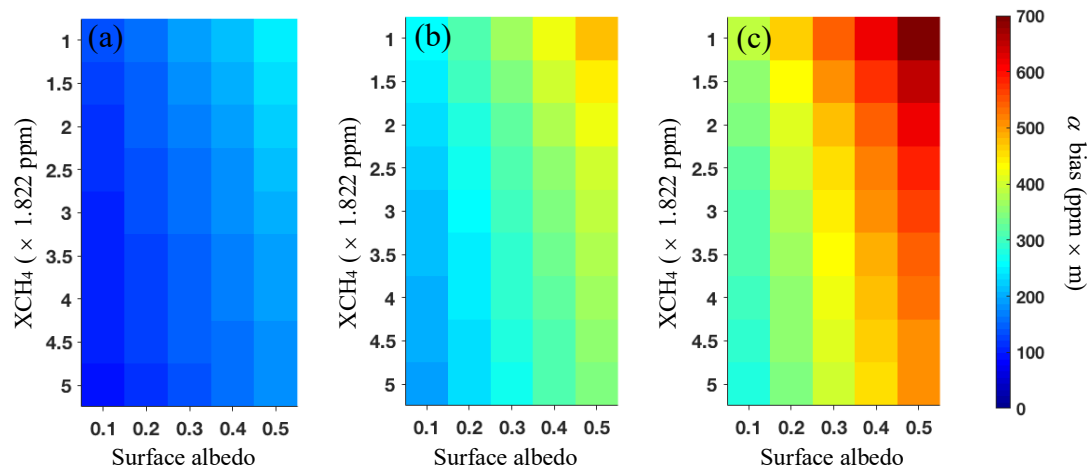
Figure 6: Bias in α as a function of XCH$_4$ and surface albedo for (a) AOD = 0.1, (b) AOD = 0.2, and (c) AOD

= 0.3.

731

732

733

734

735
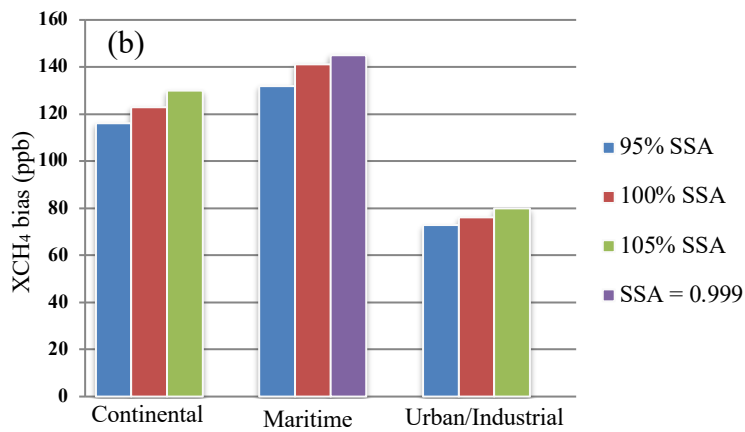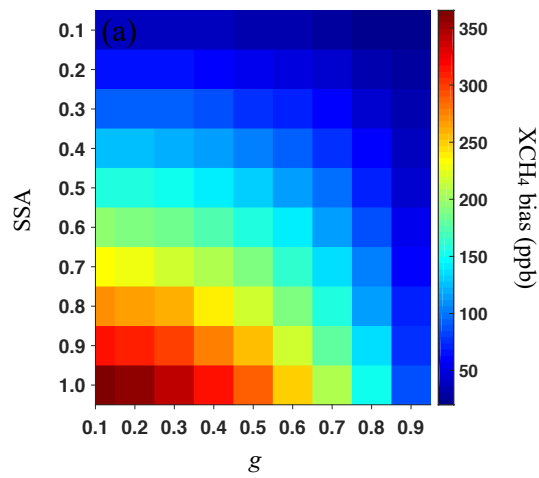
736

737
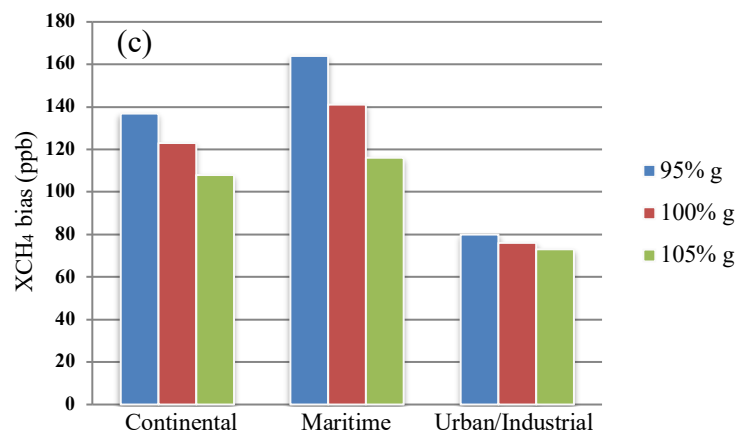
738

739 **Figure 7: (a) CH$_4$ retrieval biases for different values of *g* and SSA. Surface albedo, AOD = 0.3, XCH$_4$ = 1.0**

740 **× 1.822 ppm. (b) CH$_4$ retrieval biases for a ± 5% change in SSA for the three aerosol mixture models. (c) Same**

741 **as (b), but for a ± 5% change in *g*.**
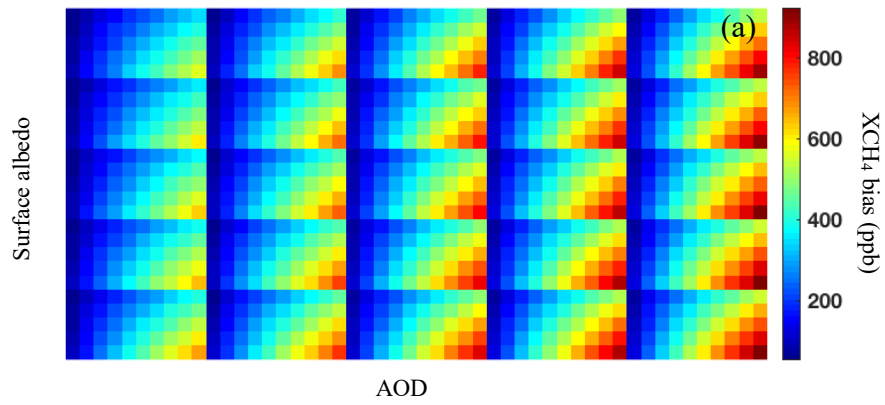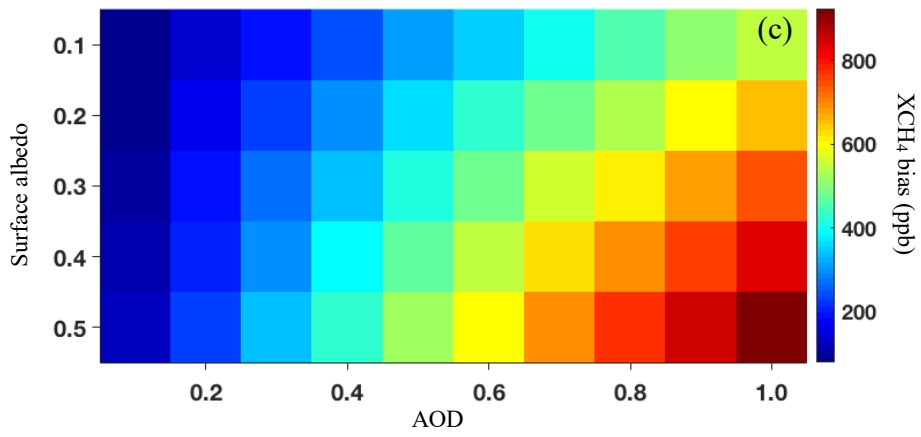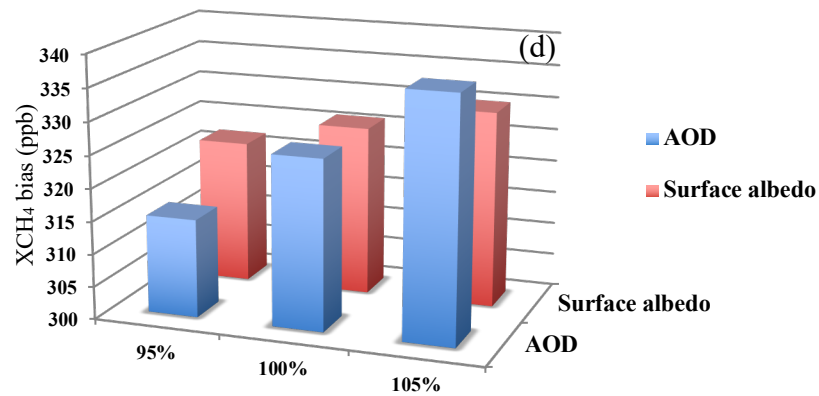
744

745 **Figure 8: (a) CH$_4$ retrieval biases for different values of XCH$_4$, AOD and surface albedo. g = 0.75, SSA = 0.95.**

746 **(b) XCH$_4$ for each box in (a). (c) Zoomed in plot of bottom right box (XCH$_4$ = 5.8 × 1.822 ppm). The x and y**

747 **axes show the variation of AOD and surface albedo, respectively. These changes are identical for every box**

748 **in (a). (d) CH$_4$ retrieval biases for a ± 5% change in AOD and surface albedo from a base value of 0.3 (g =**

749 **0.75, SSA = 0.95, XCH$_4$ = 5.8 × 1.822 ppm).**

750

751

752

753

754
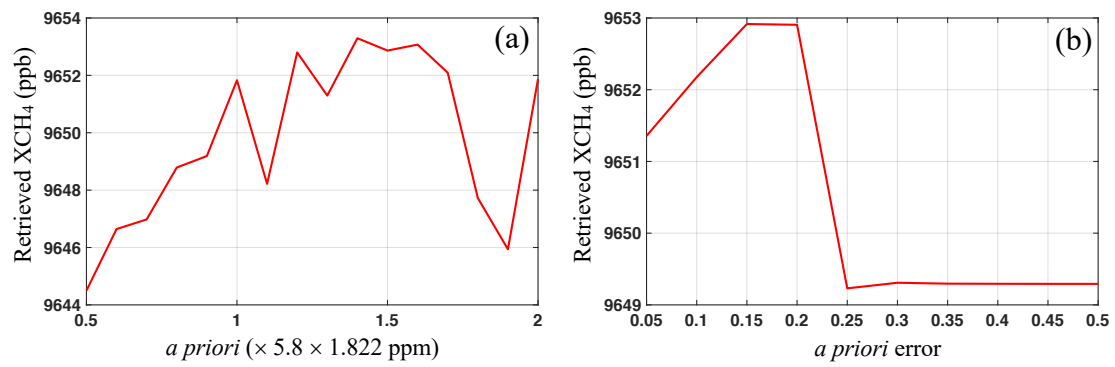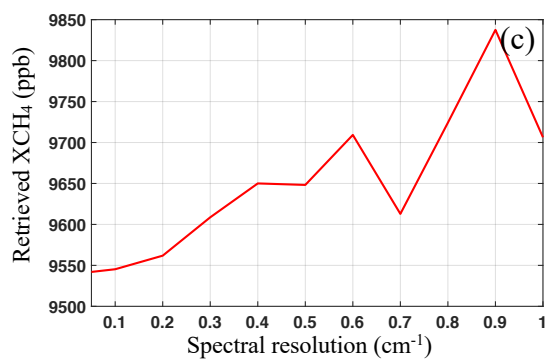
Figure 9: Retrieved XCH₄ for different values of (a) *a priori* (*a priori* error = 0.2), (b) *a priori* error (*a priori* =

5.5 × 1.822 ppm) and (c) spectral resolution. *g* = 0.75, SSA = 0.95, AOD = 1.0, surface albedo = 0.5, XCH₄ =

5.8 × 1.822 ppm.

758

759
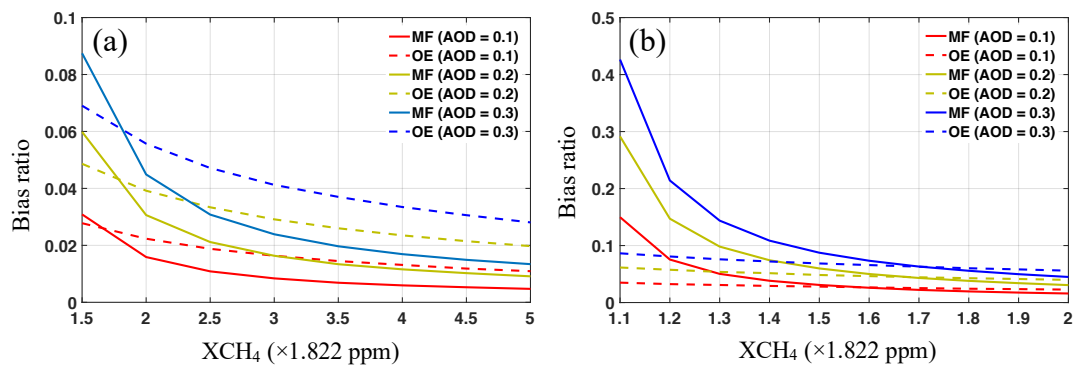
760 **Figure 10: (a) Bias ratio as a function of CH$_4$ concentration for the two retrieval techniques, where the XCH$_4$**

761 **ranges from 1.5 to 5 (× 1.822 ppm). (b) Same as (a), but for XCH$_4$ ranging from 1.1 to 2 (× 1.822 ppm). Surface**

762 **albedo is set to 0.3 for all cases; results for the MF and OE methods are shown by solid and dashed lines,**

763 **respectively.**

764

765

	Dust-like	Water soluble	Oceanic	Soot
SSA	0.805	0.799	0.970	0.014
g	0.926	0.550	0.816	0.092

766   **Table 1: Optical properties of basic aerosol types (WCRP, 1986).**

767

		Continental	Maritime	Urban/Industrial
Aerosol component	Dust-like	70%		17%
	Water soluble	29%	5%	61%
	Oceanic		95%	
	Soot	1%		22%
SSA		0.746	0.966	0.314
g		0.764	0.810	0.586

768   **Table 2: Optical properties of three aerosol mixture models (WCRP, 1986).**

769

770

Attribute	Values
Sensor height	1 km
View zenith angle	11.91°
Solar zenith angle	30.75°
Relative azimuth angle	22.87°
Aerosol loading region	surface to 1 km
SSA	0.95
g	0.75

771 **Table 3: Inputs for the 2S-ESS model simulation.**

772